1. Supplementary experiment

Synthesis of MXene

All chemicals were used as received without further purification. Layered titanium aluminium carbide Ti_3AlC_2 (MAX phase) powder was procured from Carbon-Ukraine Ltd. (particle size < 40 μm). $Ti_3C_2T_x$ (MXene) was synthesized following a MILD method [1-3]. The etching solution was prepared by adding 1.6 g lithium fluoride (LiF, 99%, Sigma-Aldrich Pty Ltd) to 20 mL 9 M hydrochloric acid (HCl), followed by stirring for 5 min to fully dissolve the LiF. 1 g of Ti_3AlC_2 powder was slowly added to the etchant at room temperature and stirred for 30 hours. The acidic suspension was washed with deionized (DI) water until pH ≈ 6 *via* centrifugation at 3500 rpm (5 min per cycle) and decanting the supernatant after each cycle. Multilayer MXene and unreacted MAX phases were removed as sediment by centrifugation at 1500 rpm for 20 min. The dark green supernatant of MXene solution that mainly contains single-layer MXene was then concentrated at 7000 rpm for 30 min. The concentration of MXene dispersion was measured by vacuum drying a specific volume of the colloidal solution (concentration 30.0 ± 0.2 mg mL^{-1}).

2. Supplementary results

Isotropic to nematic (I-N) transition concentration in lyotropic liquid crystalline MXene dispersions

It was previously shown that for disk-shaped particles, the isotropic-nematic (I-N) transition occurs when the dimensionless density of nw^3 is 4.12 (n denotes the number density of disks per unit area and w denotes the diameter of the disk-shaped particle)[4]. Assuming MXene flakes as disk-shaped particles, the volume of single MXene flakes (V) can be obtained using the Equation S1.

$$V = \frac{\pi w^2 t}{4} \tag{S1}$$

In this equation t is the thickness of the MXene flakes. At the I-N transition, the mass concentration (c) of the MXene dispersion can be obtained by the Equation S2 using the density (ρ) of the MXene flakes.

$$n = \frac{c}{V\rho} \tag{S2}$$

We used ~5.15 g cm^{-3} for the density of Ti_3C_2, which is the theoretical density of MXene flakes[5]. Using Equations S1 and S2, nw^3 can be obtained as follows:

$$nw^3 = \frac{cw^3}{V\rho} = \frac{cw^3}{\frac{\pi w^2 t}{4}\rho} = \frac{4c\alpha}{\pi\rho} = 4.12 \tag{S3}$$

Where α is obtained by dividing the MXene width (w) over its thickness (t). Hence the theoretical MXene concentration at the I-N transition can be obtained using the Equation S4.

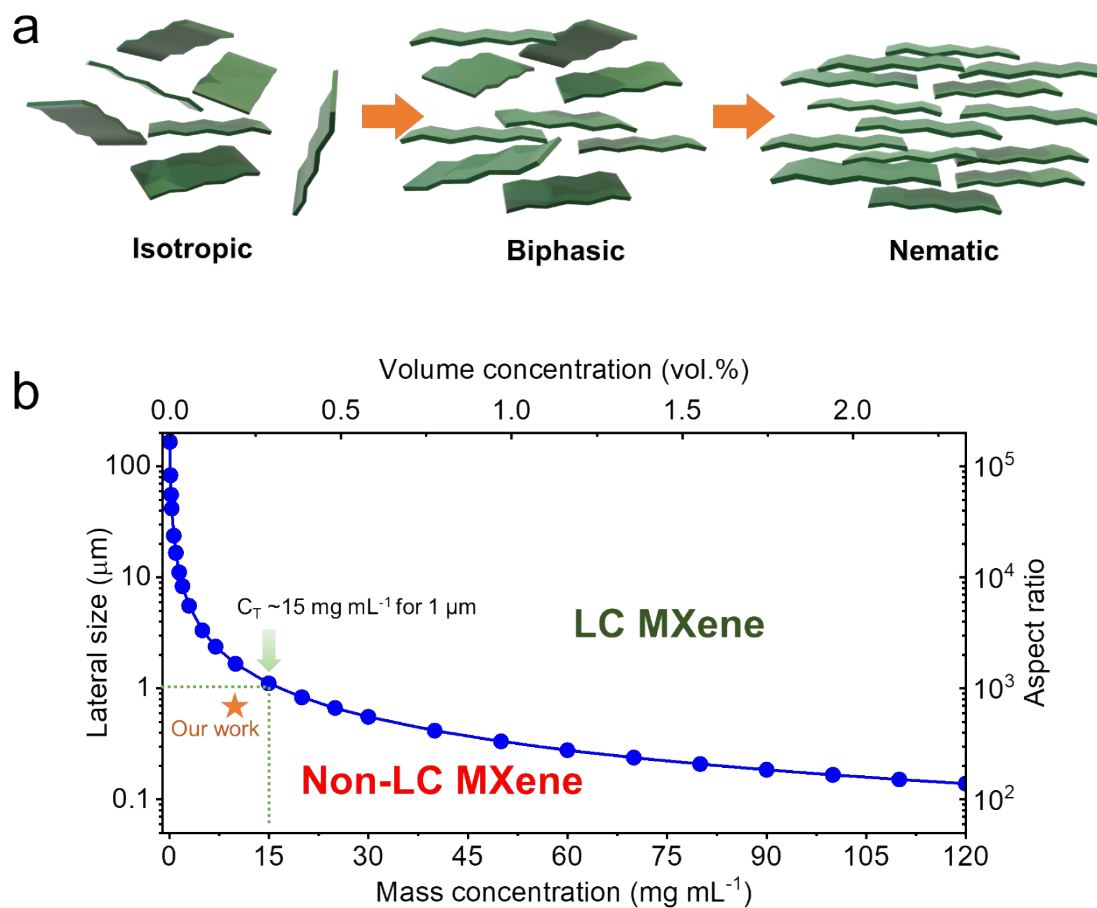$$c = 1.03\frac{\pi\rho}{\alpha} \tag{S4}$$

Fig. S1. (a) Schematic diagram showing the transformation of isotropic MXene phases into Nematic LC phase. (b) A plot based on Onsager's Theory predicting which concentration (either mass or volume) a particular MXene flake size would exhibit LC behaviour.

Validation of MXene Synthesis

Atomic force microscopy (AFM) images were obtained using ScanAsyst atomic force microscopy scan mode (Bruker MultiMode 8-HR) to measure the flake thickness. AFM samples were prepared by drop casting a MXene solution on silicon wafers. XRD patterns were recorded with a powder diffractometer (PANalytical X'Pert Powder) using Cu Kα radiation (λ = 1.54 Å) at a 2θ scan step of 0.013° and 100 milliseconds dwell time. XRD samples were prepared by mounting the films on a zero background SiO_2 substrate. The SEM images (Figure S1a and S1b) suggest that the solid MAX phases were effectively etched and exfoliated into single/few-layer MXene sheets, with varying sheet-sizes. The removal of the "A" layer was also confirmed using XRD where the (104) diffraction peak for MAX phase, corresponding to Al was no longer visible after etching (Figure S1c). Similarly, the prominent (002) diffraction of MAX at ~9.5° reduced to 7.0°, consistent with MXene, indicative of an increase in inter-layer spacing brought about by exfoliation of single-layer MXene sheets. As quantified using Bragg's law, the shift of the (002) plane corresponded to an increased inter-planar distance from 0.92 nm to 1.26 nm after etching.
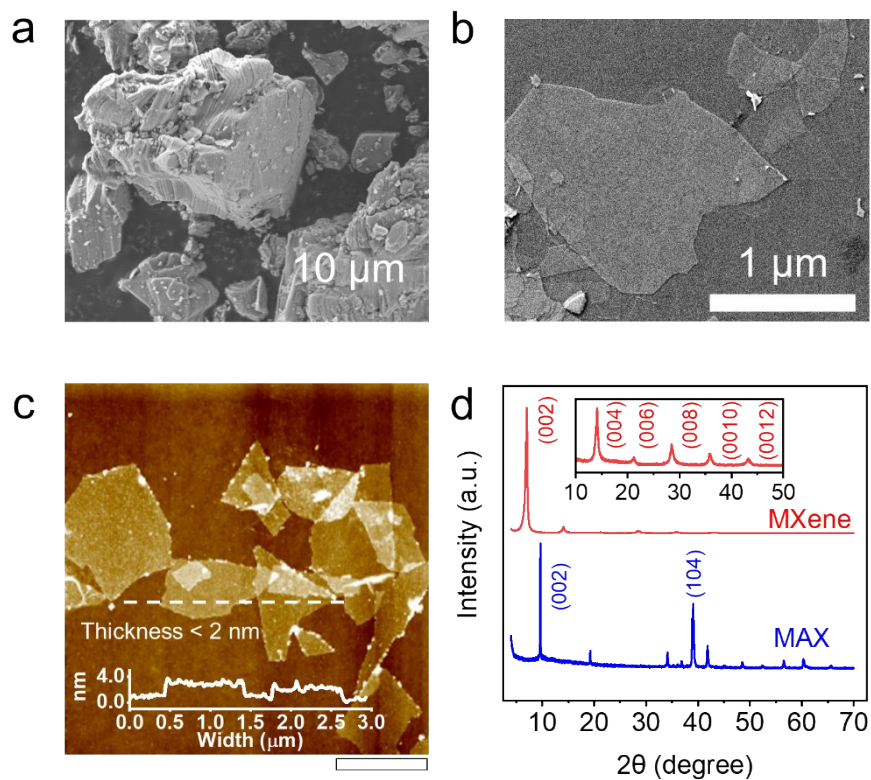
Fig. S2. Validation of $Ti_3C_2T_x$ MXene synthesis. SEM images of (a) Ti_3AlC_2 (MAX phase) and (b) $Ti_3C_2T_x$ MXene obtained through the MILD method. (c) Atomic Force Microscope (AFM) image of MXene (d) XRD spectra of MAX and MXene. The (104) diffraction of MAX phase disappeared after etching and the (002) diffraction downshifted providing evidence for removal of Al and delamination of MXene respectively.
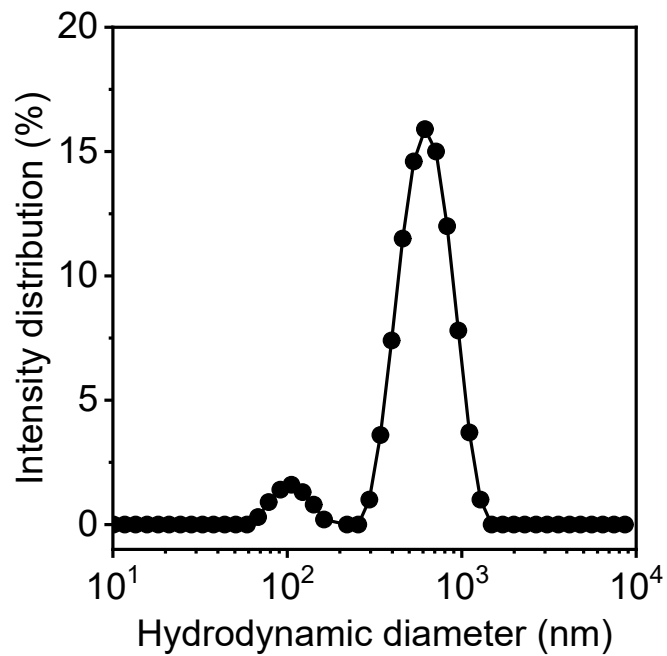
Fig. S3. Estimation of average MXene flake size using DLS showing that the acquired MXene dispersion consists of flakes with lateral sizes of < 1 μm.
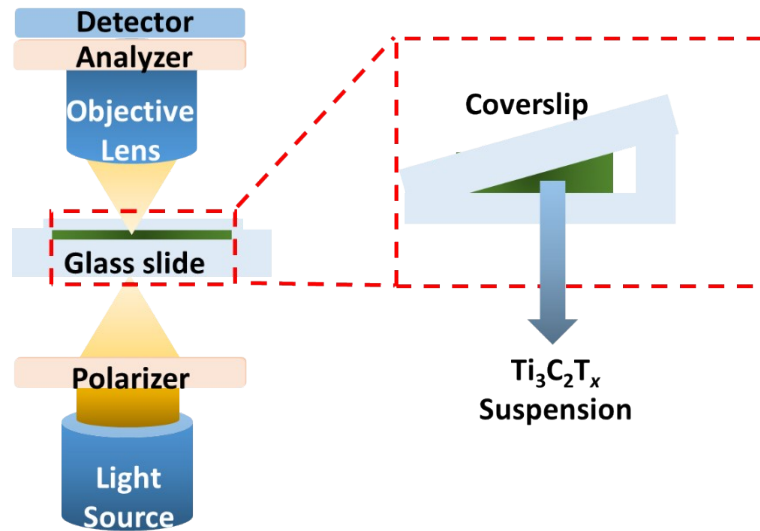
Fig. S4. Schematic illustration of the setup used for polarized optical microscopy (POM) to observe the nematic phase in MXene dispersions.
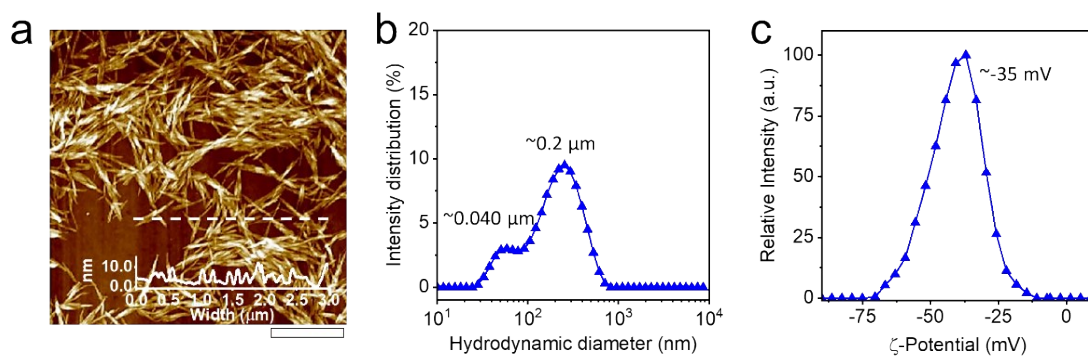

Fig. S5. (a) AFM Image, (b) DLS size distribution profile, and (c) ζ-potential of CNC
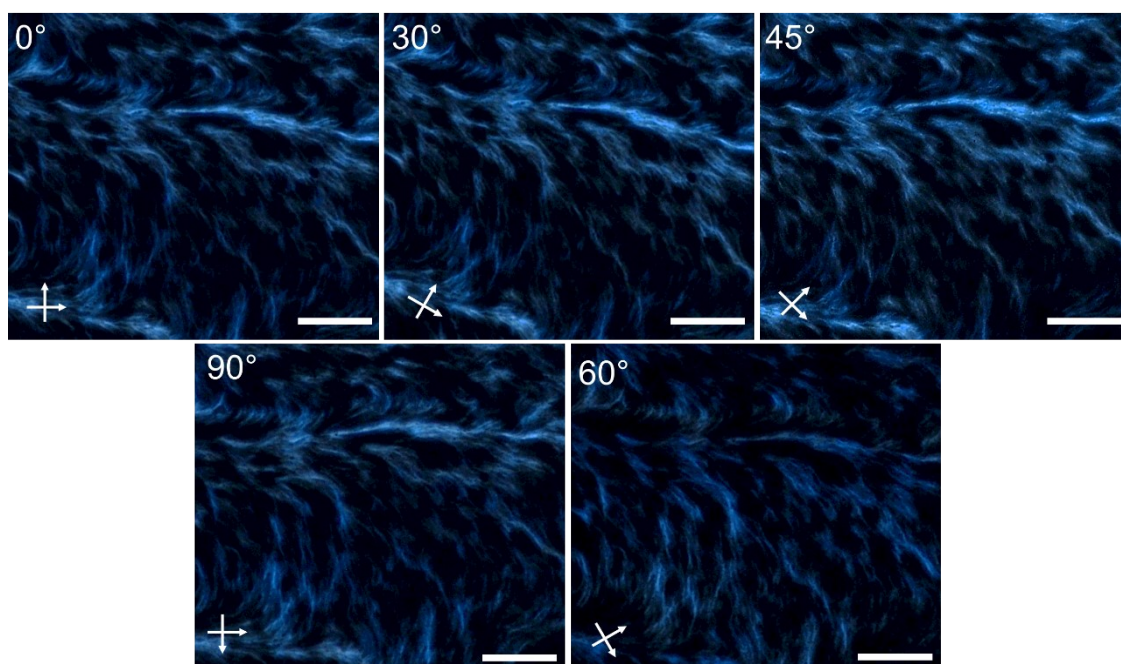
Fig. S6. Birefringence of 30 mg mL^{-1} LC-MXene dispersion observed under POM showing changes in intensity and brightness of the Schlieren textures upon rotating the polarizer and analyser in crossed configuration (40x magnification). All scale bars in figures are 100 μm.
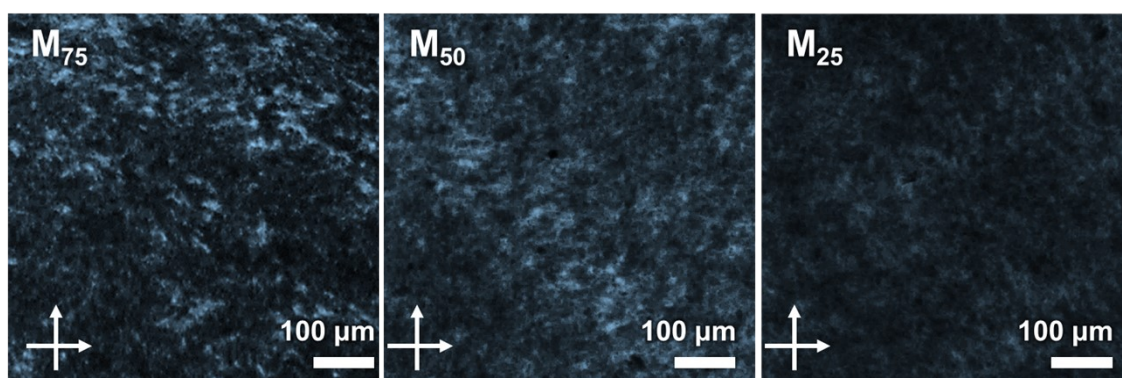

Fig. S7. Birefringence patterns of M$_{75}$, M$_{50}$ and M$_{25}$ MXene dispersions, showing the appearance of Schlieren textures for all samples. All scale bars in figures are 50 μm.
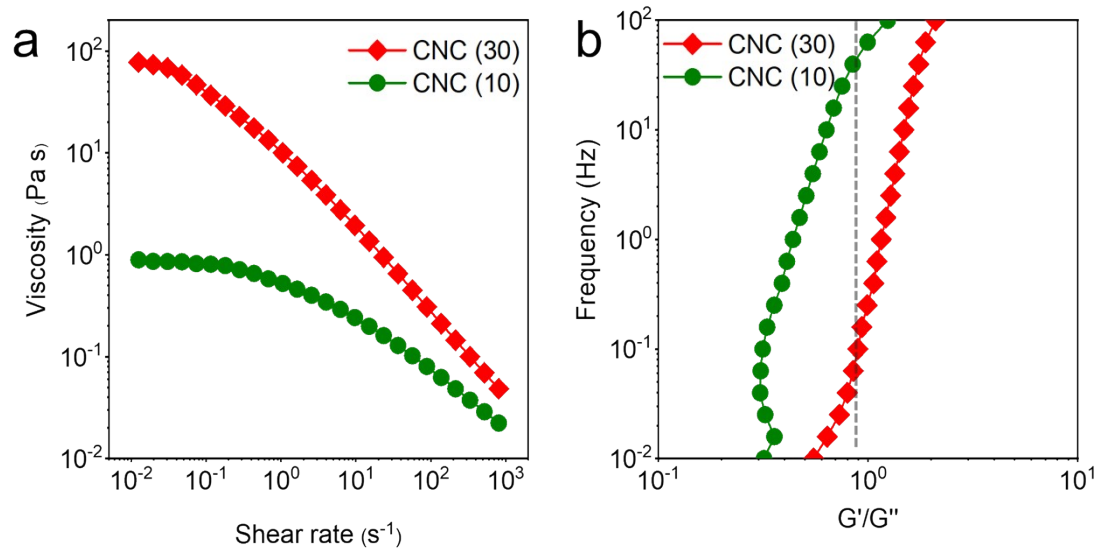
Fig. S8. Rheological properties of 30 mg mL^{-1} and 10 mg mL^{-1} CNC dispersions. (a) Viscosity vs. shear rate plot, (b) G'/G" ratios at varying oscillation frequencies (Hz).

Table S1. Summary of MXene, CNC and MXene-CNC dispersions showing the exact volumes and concentrations used in this experiment.

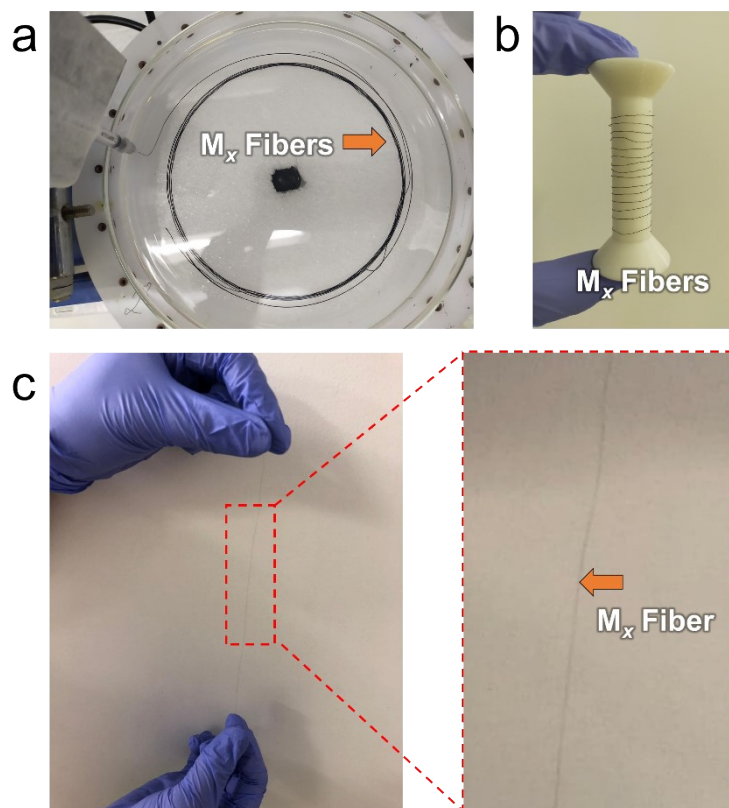| Sample Name	MXene		CNC		Water	Effective Concentration			LC Behaviour	Spinnable
	Conc. (mg mL^{-1})	Vol. (mL)	Conc. (mg mL^{-1})	Vol. (mL)	Vol. (mL)	MXene (mg mL^{-1})	CNC (mg mL^{-1})	Total Solid (mg mL^{-1})		
M$_{100}$	10	1	~	~	~	10	~	**10**	No	No
M$_{75}$	10	1.5	30	0.167	0.333	7.5	2.5	**10**	Yes	Yes
M$_{50}$	10	1.00	30	0.333	0.667	5	5	**10**	Yes but weak	Yes
M$_{25}$	10	0.5	30	0.5	1	2.5	7.5	**10**	Yes but weak	Yes
CNC (10)	~	~	10	1	~	~	10	**10**	No	No
H M$_{100}$	30	1	~	~	~	30	~	**30**	Yes	Yes
H M$_{75}$	30	0.5	30	0.167	0	22.5	7.5	**30**	Yes	Yes
H M$_{50}$	30	0.33	30	0.33	0	15	15	**30**	Yes	Yes
H M$_{25}$	30	0.167	30	0.5	0	7.5	22.5	**30**	Yes	Yes
CNC (30)	~	~	30	1	~	~	30	**30**		Yes
CNC (40)	~	~	40	1	~	~	40	40	No	Yes
CNC (50)	~	~	50	1	~	~	50	**50**	Yes	Yes

Fig. S9. Wet-spinning of M_x fibers (a) Photograph showing the coagulation of gel-state MXene-CNC blend, (b) Spool acquired after drawing the fibers out of the coagulation bath followed by drying. (c) Handling of individual M_x fiber.
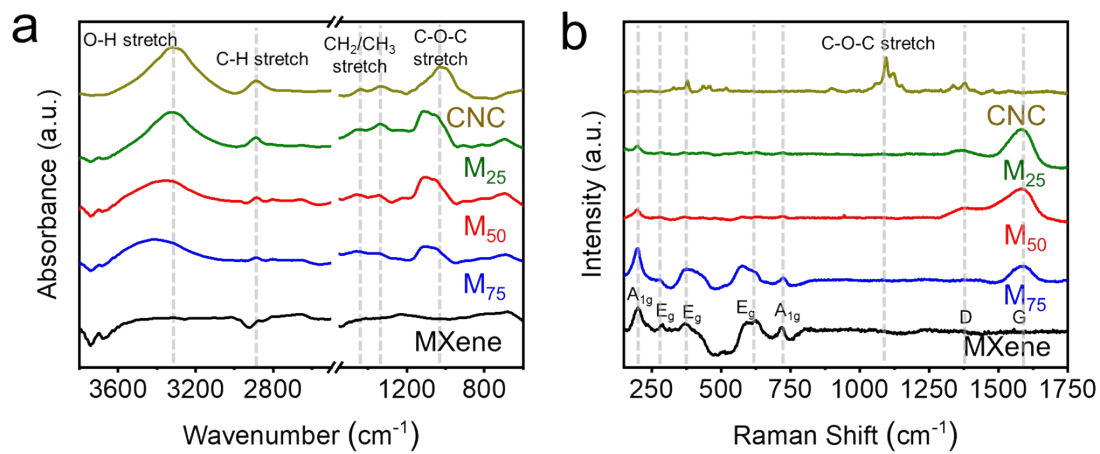
Fig. S10. Chemical profiles of MXene, CNC and MXene CNC blends acquired using (a) FTIR and (b) Raman spectroscopies.
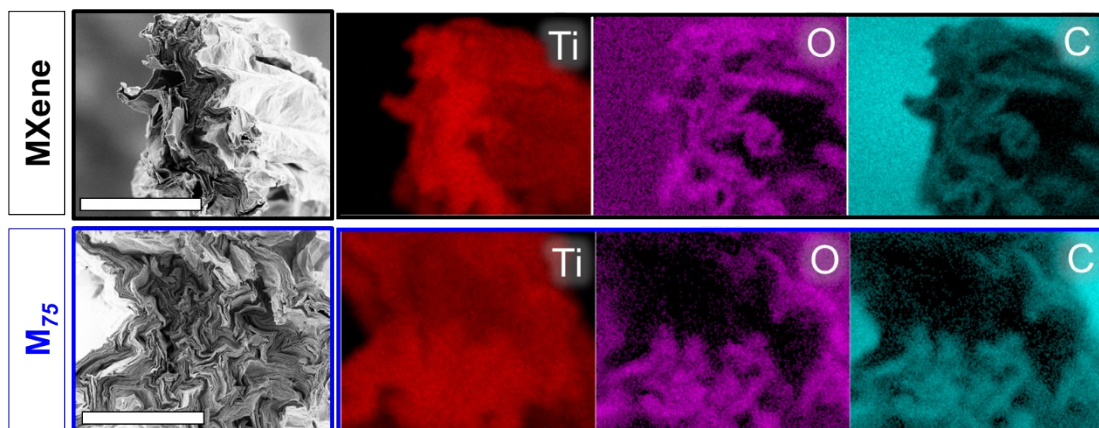
Fig. S11.   EDX maps of pure MXene and *H* M$_{75}$ fibre cross-sections. Ti, O and C maps indicate that there is no distinct layers formed in between the Ti groups implying that the C-rich CNC is evenly distributed in the material.
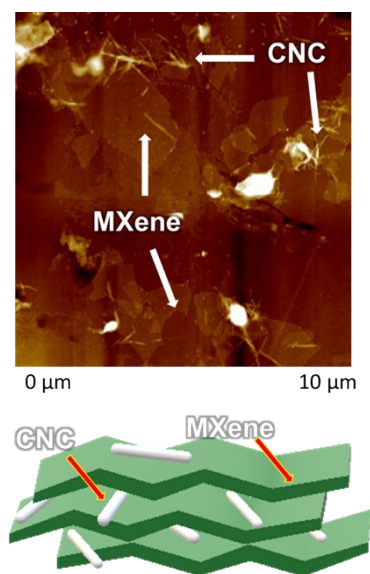
Fig. S12.   Since the MXene surface is not saturated as shown in the AFM image, the effect of CNC insertion on the *d*-spacing is expected to be not very prominent, therefore what we effectively see in the WAXS profile is the spacing in between the contacting nanosheets. The microstructure caused by the attachment of CNC onto MXene is however cannot be detected in the WAXS region but could be better seen in the SAXS region.
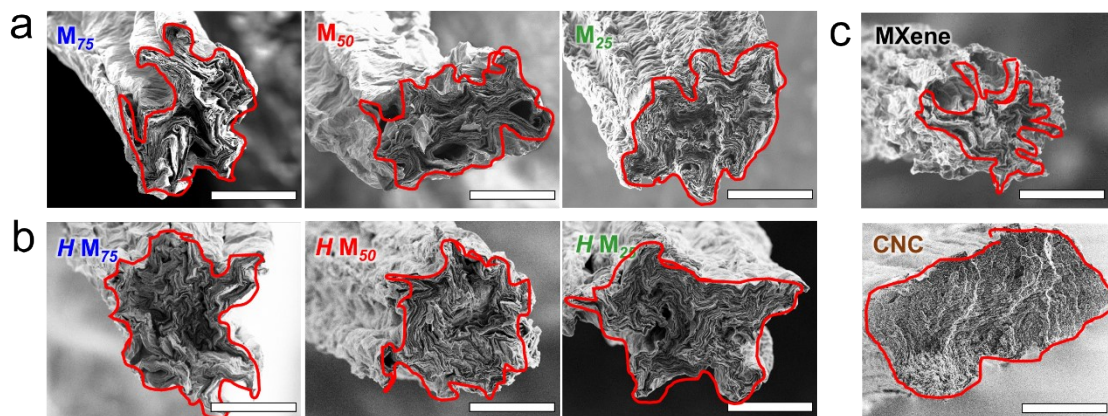

Fig. S13.   Cross-sectional SEM images of microfibers showing the effective area used in the calculation of physical and electrochemical properties.
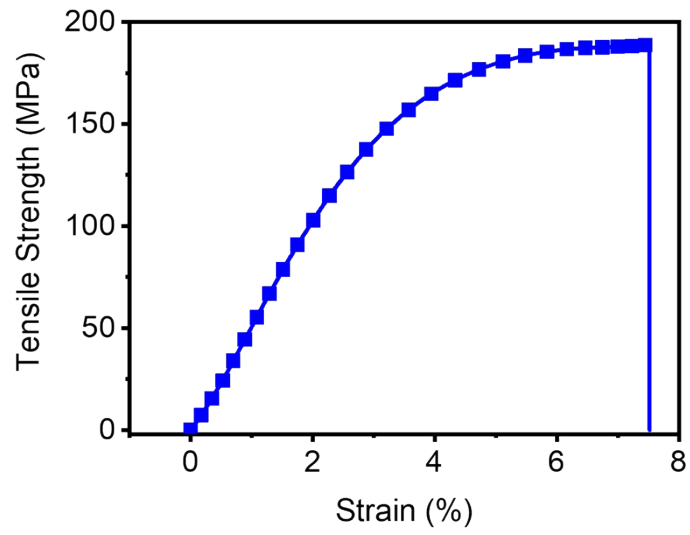
Fig. S14. Representative stress-strain curve showing the mechanical property of pure CNC fiber.
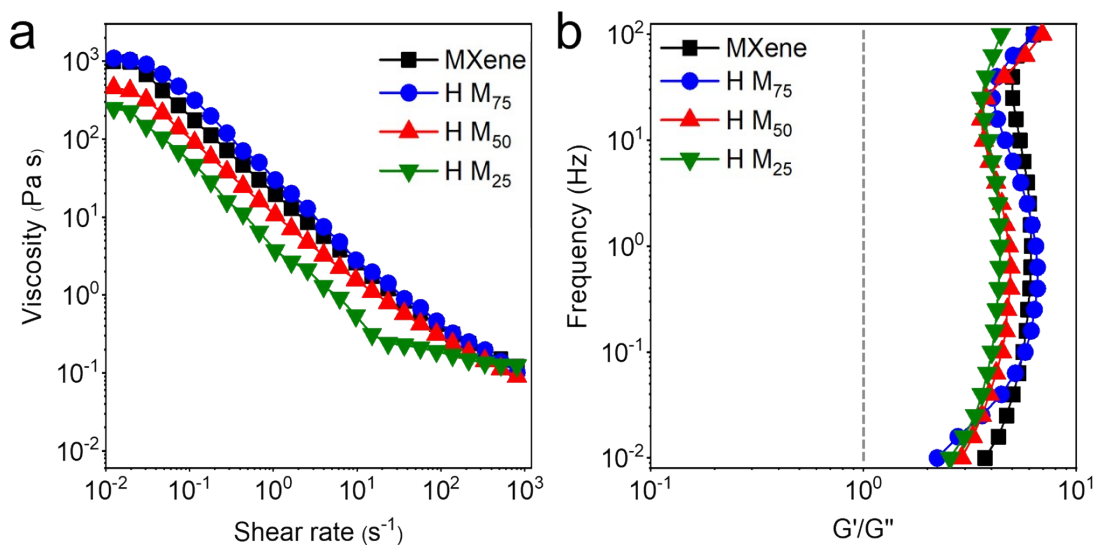
Fig. S15. Rheological properties of MXene-CNC dispersions at high total solid concentration (30 mg mL^{-1}) showing (a) Viscosity versus shear rate relationships, (b) viscoelastic behavior showing the frequency dependence of elastic over viscous modulus ratios (G'/G"). The right side of the dashed line (G'/G" ratio > 1) indicates dispersions with viscoelastic gel-like properties.
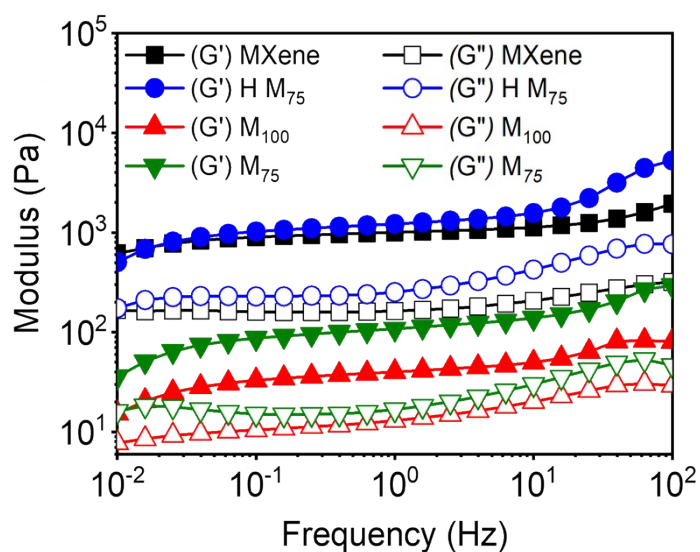

Fig. S16. Viscoelastic Properties of M$_x$ and HM$_x$ dispersions showing the dominance of G' over G" for all samples, indicating excellent viscoelastic behaviour. The higher G'/G" implies that the aligned structure acquired during wet spinning can be retained upon removal of shear forces.
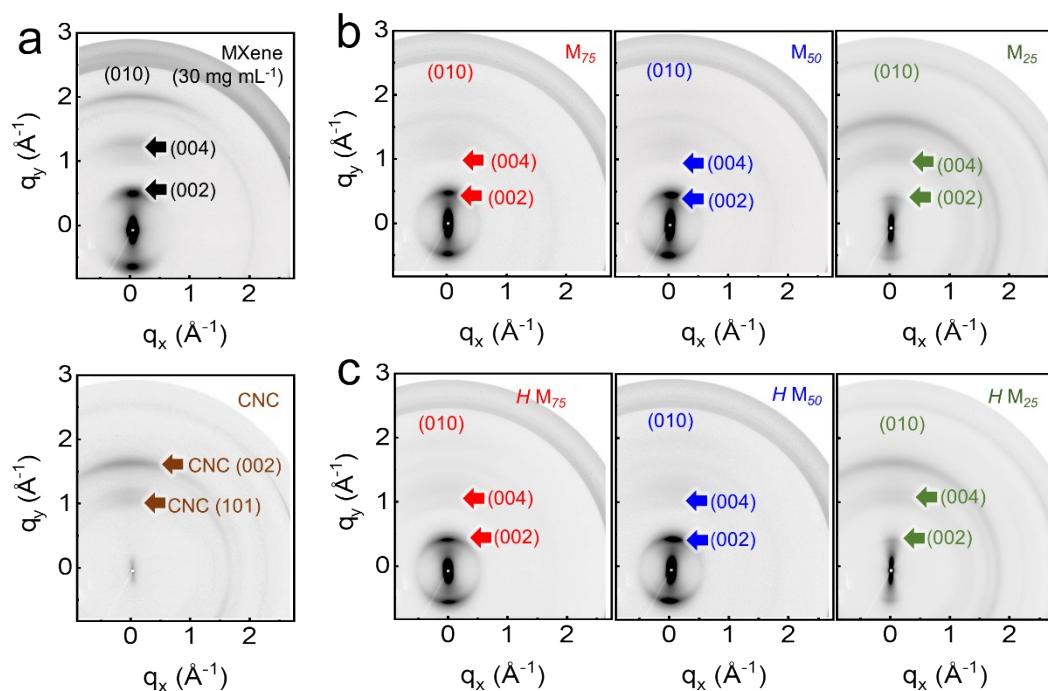
Fig. S17. SAXS/WAXS profile of all fibres *(Summary)*. (a) MXene and CNC, and (b-c) MXene-CNC blends showing 1) MXene scattering patterns at $q = 0.55$ Å^{-1} and $q = 2.41$ Å^{-1}, attributable to the presence of the (002) and (010) peak of MXene 2) CNC (101) and (002) scatterings at $q = 1.00$ Å^{-1} and $q = 1.50$ Å^{-1}.
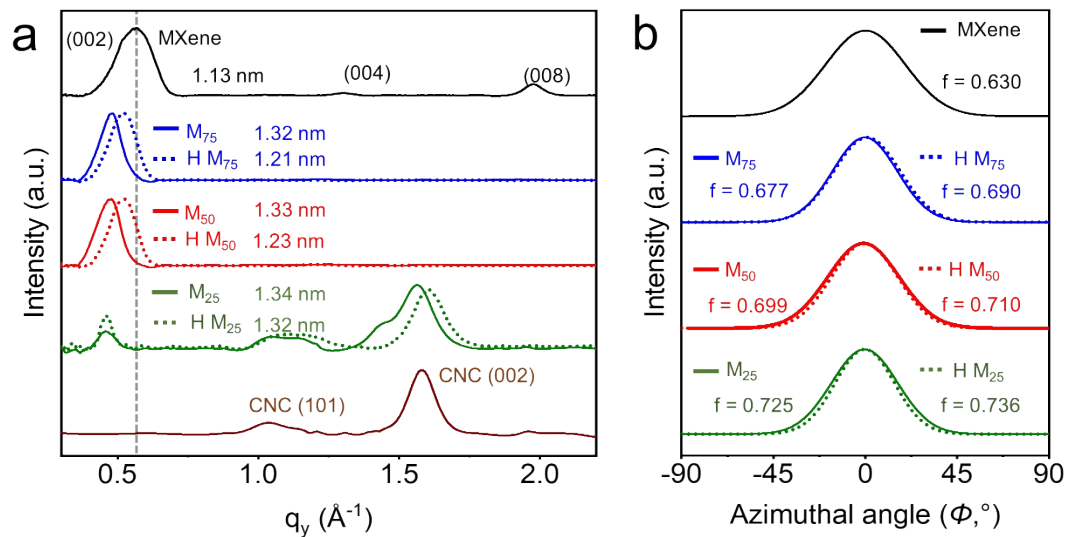
Fig. S18.　SAXS/WAXS diffractograms of all fibers *(Summary)* (a) Diffractograms of the fiber samples obtained by integration of SAXS/WAXS spectra shown along the q_y direction. (b) Diffractograms of the fiber samples obtained by integration of SAXS/WAXS 2D spectra shown in (a) along the q_y direction.
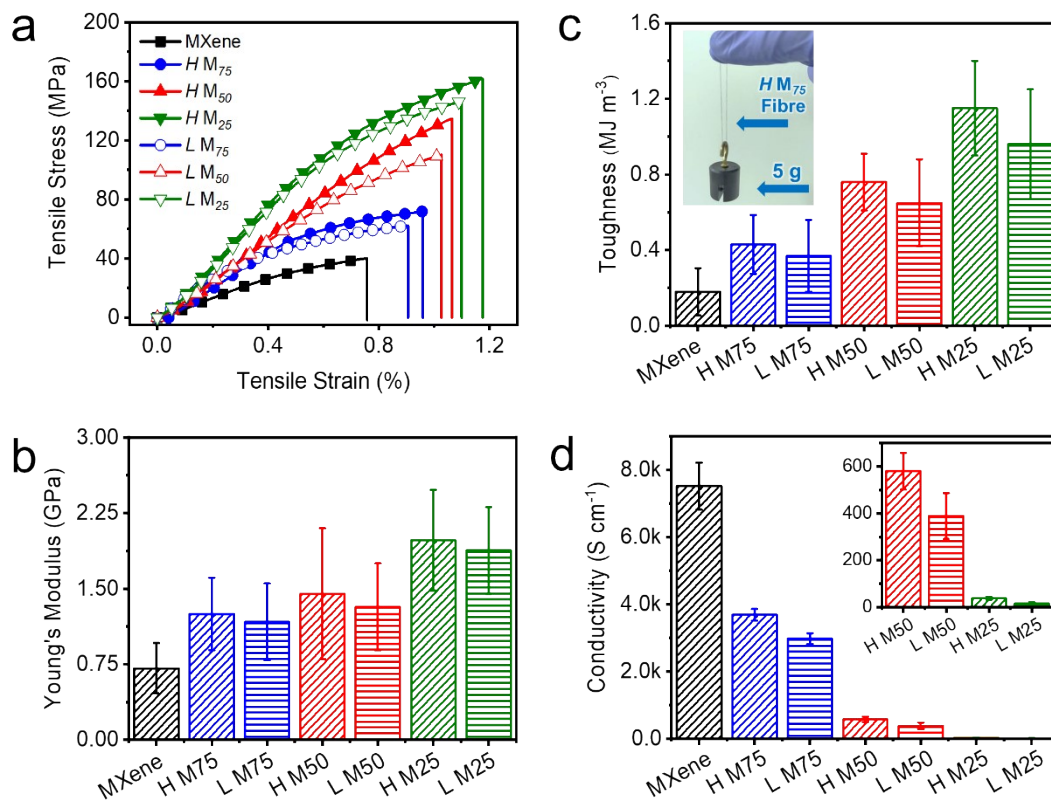
Fig. S19. Mechanical properties of all wet-spun fibers *(Summary)*. (a) Representative stress-strain curves, (b) average Young's modulus and (c) average toughness of microfibers made from mixed systems with low and high concentration total solids. (d) Electrical conductivity of the wet-spun fibers calculated based on cross-sectional area measured from SEM.
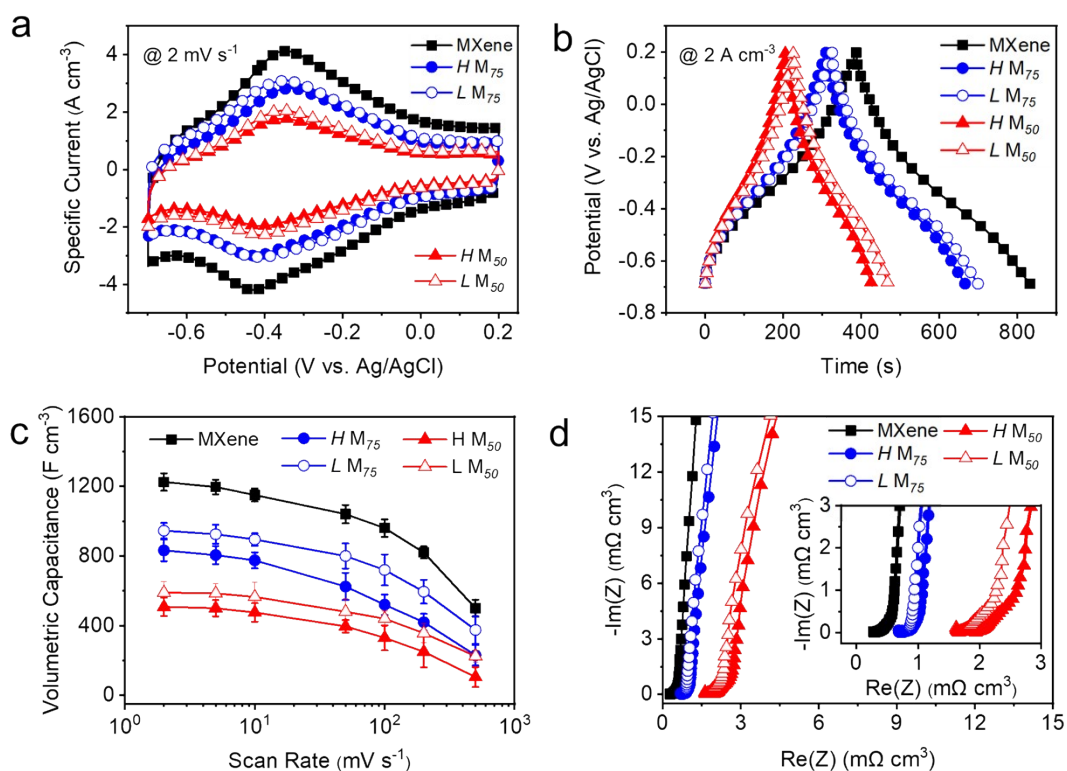
Fig. S20. Electrochemical performance of all wet-spun fibers *(Summary)*. (a) CV at scan rate of 2 mV s^{-1} and (b) GCD curves at 2 A cm^{-3}. (c) The values of volumetric capacitance of MXene fiber electrodes as a function of increased at scan rates from 2 mV s^{-1} to 500 mV s^{-1} (d) Nyquist plots of the MXene fiber electrodes acquired from the EIS data. The resistance values are normalized over the volume of the electrode with inset showing the high frequency EIS region.

Table S2. Electrical, mechanical, and electrochemical properties of selected wet-spun MXene-based fibers in the current literature

Type of Fiber	MXene loading (wt. %)	Diameter [μm]	Conductivity [S cm^{-1}]	Tensile strength [MPa]	Strain-to-failure [%]	Volumetric capacitance C_v [F cm^{-3}]	Areal capacitance C_a [mF cm^{-2}]	Gravimetric capacitance C_g [F g^{-1}]	Linear capacitance C_L [mF cm^{-1}]	Ref.
LC-MXene fiber	100	~30	7,512	40	0.75	1,225	~	~	~	This work
MXene/CNC L M$_x$C$_y$ fibers	75 50 25	~40	2,978 389 15	62 109 145	0.9 1.02 1.1	945 590 ~	~	~	~	This work
MXene/CNC H M$_x$C$_y$ fibers	75 50 25	~40	3,692 580 38	75 134 160	0.96 1.05 1.18	832 508 ~	~	~	~	This work
LC-MXene fiber	100	~50	7,748	40.5	1.7	1265	1762	393	~	6
LC-MXene fiber	100	~40	7,713	63.9	0.22	~	~	~	~	7
MXene gel fiber	100	~10	12,504	343.68	0.28	~	~	~	~	8
MXene/ poly(3,4-ethylenedioxythiophene (PEDOT) fiber	70	~20	1,489	58.7	<2	615	676	258	4.6	1
MXene/rGO fiber	88	~70	72.3	132.5	2.9	341	233	257	~1.2	9
MXene/rGO fiber	90	~30	290	12.9	~3.75	891	565	495	~	10
MXene/ polycaprolactone fiber	30	~130	~0.002	4.15	770	~	~	~	~	3
MXene/polyurethane coaxial fiber	1	~50-100	10^{-5}	~40	~400	~	~	~	~	11

References

1.   Zhang, J.;   Seyedin, S.;   Qin, S.;   Wang, Z.;   Moradi, S.;   Yang, F.;   Lynch, P. A.; Yang, W.;   Liu, J.;   Wang, X.; Razal, J. M., Highly Conductive Ti3C2Tx MXene Hybrid Fibers for Flexible and Elastic Fiber-Shaped Supercapacitors. *Small* **2019,** *15* (8), 1804732.

2.   Wang, Z.;   Qin, S.;   Seyedin, S.;   Zhang, J.;   Wang, J.;   Levitt, A.;   Li, N.;   Haines, C.;   Ovalle-Robles, R.;   Lei, W.;   Gogotsi, Y.;   Baughman, R. H.; Razal, J. M., High-Performance Biscrolled MXene/Carbon Nanotube Yarn Supercapacitors. *Small* **2018,** *14* (37), 1802225.

3.   Seyedin, S.;   Zhang, J.;   Usman, K. A. S.;   Qin, S.;   Glushenkov, A. M.;   Yanza, E. R. S.;   Jones, R. T.; Razal, J. M., Facile Solution Processing of Stable MXene Dispersions towards Conductive Composite Fibers. *Global Challenges* **2019,** *3* (10), 1900037.

4.   Forsyth, P. A.;   Marčelja, S.;   Mitchell, D. J.; Ninham, B. W., Onsager transition in hard plate fluid. *Journal of the Chemical Society, Faraday Transactions 2: Molecular and Chemical Physics* **1977,** *73* (1), 84-88.

5.   Mashtalir, O., *Chemistry of two-dimensional transition metal carbides (MXenes)*. Drexel University: 2015.

6.   Zhang, J.;   Uzun, S.;   Seyedin, S.;   Lynch, P. A.;   Akuzum, B.;   Wang, Z.;   Qin, S.; Alhabeb, M.;   Shuck, C. E.;   Lei, W.;   Kumbur, E. C.;   Yang, W.;   Wang, X.;   Doin, G.; Razal, J. M.; Gogotsi, Y., Additive-Free MXene Liquid Crystals and Fibers. *ACS Cental Science* **2020,** *Just Accepted*.

7.   Eom, W.;   Shin, H.;   Ambade, R. B.;   Lee, S. H.;   Lee, K. H.;   Kang, D. J.; Han, T. H., Large-scale wet-spinning of highly electroconductive MXene fibers. *Nat. Commun.* **2020,** *11* (1), 2825.

8.   Shin, H.;   Eom, W.;   Lee, K. H.;   Jeong, W.;   Kang, D. J.; Han, T. H., Highly Electroconductive and Mechanically Strong Ti3C2Tx MXene Fibers Using a Deformable MXene Gel. *ACS Nano* **2021,** *15* (2), 3320–3329.

9.   Seyedin, S.;   Yanza, E.; Razal, J. M., Knittable energy storing fiber with high volumetric performance made from predominantly MXene nanosheets. *J. Mater. Chem. A* **2017,** *5* (46), 24076-24082.

10.   Yang, Q.;   Xu, Z.;   Fang, B.;   Huang, T.;   Cai, S.;   Chen, H.;   Liu, Y.;   Gopalsamy, K.;   Gao, W.; Gao, C., MXene/graphene hybrid fibers for high performance flexible supercapacitors. *J. Mater. Chem. A* **2017,** *5* (42), 22113-22119.

11.   Seyedin, S.;   Uzun, S.;   Levitt, A.;   Anasori, B.;   Dion, G.;   Gogotsi, Y.; Razal, J. M., MXene Composite and Coaxial Fibers with High Stretchability and Conductivity for Wearable Strain Sensing Textiles. *Adv. Funct. Mater.* **2020,** *30* (12), 1910504.